Unveiling the interplay of magnetic order and electronic band structure in the evolution of the anomalous Hall effect in single crystalline MnPtGa

Gourav Dwari [1,*] Shovan Dan [1,2] Bishal Baran Maity [1] Sitaram Ramakrishnan [3,4] Achintya Lakshan [5] Ruta Kulkarni [1] Vikash Sharma [1] Suman Nandi [1] Partha Pratim Jana [5] Andrzej Ptok [6,†] and A. Thamizhavel [1,‡]

[1]*Department of Condensed Matter Physics and Materials Science, Tata Institute of Fundamental Research, Homi Bhabha Road, Colaba, Mumbai 400005, India*

[2]*Institute of Low Temperature and Structure Research, Polish Academy of Sciences, Okólna 2, 50-422 Wrocław, Poland*

[3]*Department of Quantum Matter, AdSE, Hiroshima University, 739-8530 Higashi-Hiroshima, Japan*

[4]*I-HUB Quantum Technology Foundation, Indian Institute of Science Education and Research, Pune 411008, India*

[5]*Department of Chemistry, IIT Kharagpur, Kharagpur 721302, India*

[6]*Institute of Nuclear Physics, Polish Academy of Sciences, W. E. Radzikowskiego 152, PL-31342 Kraków, Poland*

(Received 22 April 2024; accepted 11 June 2024; published 8 July 2024)

The recent studies on the anomalous Hall effect (AHE) have revealed an intrinsic relationship between the topological band structure and the experimentally observed transverse conductivity. Consequently, this has led to a heightened focus on examining the topological aspects of AHE. Here, an in-depth study of temperature driven sign reversal of anomalous Hall conductivity in the single crystalline MnPtGa (space group: $P6_3/mmc$) has been presented. From the interdependence of the linear and anomalous Hall resistivity, the origin of AHE is confirmed to be of intrinsic type. By systematically studying the electronic band structure and Berry curvature of MnPtGa using first principle calculations supported by temperature and magnetic field dependent magnetization measurements, it is concluded that the temperature dependent complex magnetic structure plays a significant role and leads to the sign reversal of anomalous Hall conductivity. Supported by the *ab initio* calculations, a continuous evolution of the magnetic structure is proposed, which is consistent with the experimental data. This study has established that the critical temperature (≈110 K), where the sign reversal appears is strongly associated with the magnetic structure and the magnitude of Mn moments.

DOI: 10.1103/PhysRevB.110.045111

I. INTRODUCTION

Although identified long ago, the complete understanding of the anomalous Hall effect (AHE), involving time-reversal symmetry breaking, is yet to be resolved. Primarily, it was argued to originate from intrinsic or extrinsic contributions [1]. Intrinsic AHE originates from the magnetism, band topology, Berry curvature, etc. [2–4]. Extrinsic AHE, on the other hand, originates from scattering mechanisms like skew scattering and side jump due to spin-orbit interaction [5–7]. Despite its complex origins, the anomalous Hall resistivity (ρ_{xy}^{A}) exhibits a striking association with the linear resistivity (ρ_{xx}) through a power-law relationship, $\rho_{xy}^{A} \propto \rho_{xx}^{\beta}$. This interconnection holds crucial implications for understanding the underlying mechanisms of the AHE [1,8]. Depending on the values of the exponent β, it was argued to originate from the intrinsic or extrinsic mechanism. Nevertheless, a subsequent theoretical model was proposed to support the experimental observation of the AHE. Moreover, the specific topological band involved in the electronic structure plays a crucial role in determining both the magnitude and sign of the anomalous Hall conductance (AHC) in the intrinsic AHE. Depending on the position of the band, or the modification of the band by the external parameters, the values of the AHC may change by a significant amount. Such phenomena were observed in a series of metallic compounds, viz., $Co_3Sn_2S_2$ [9,10], Co_2MnGa [11], and Fe_3GeTe_2 [12]. An alteration in the sign was noted in a Weyl semimetal, HoPtBi, and it was suggested that this was caused by the splitting of Weyl nodes, which is modulated by exchange splitting [13].

The sign change in AHC has also been observed in epitaxial thin films of La-doped $EuTiO_3$, irrespective of the synthesis conditions [14]. In that case, the change of sign was attributed to the chemical potential shift (as a function of the magnetic field). Probably, the most interesting observation of the AHE was reported in the itinerant ferromagnet $SrRuO_3$, where the variation of the AHC was observed as a function of temperature. A correlation between structure and magnetism was discussed to draw a link with the magnetic monopole [15]. A similar discussion on the monopole and the Berry curvature was discussed for the compound $Co_3Sn_2S_2$ [10]. Reports also suggest that it is possible to tune the AHE in compounds by doping, so that the Fermi level lies between the overlap of two narrow bands which leads to a change in sign of effective spin-orbit parameter resulting in a sign reversal of AHC as observed in semiconducting family $BaFe_{2\pm x}Ru_{4\mp x}O_{11}$ [16] and metallic spinel $CuCr_2Se_{4-x}Br_x$

*Contact author: gourav.dwari@tifr.res.in
†Contact author: aptok@mmj.pl
‡Contact author: thamizh@tifr.res.in

[17]. However, such mechanism does not result a nonmonotonicity in AHC.

The AHE in thin films of MnPtGa was recently reported to exhibit a strict nonmonotonic behavior and it was claimed that the sign reversal (≈110 K) of AHC is very robust with temperature, and the variation in thickness does not affect this phenomenon [18]. Although, the authors of Ref. [18] performed a temperature-dependent neutron diffraction (ND) study of the compound [19], the justification for the robustness of the temperature at which the sign of AHC reverses still remains unsolved. For the same compound, in polycrystalline form, a serious ND study was performed, notwithstanding the focus was different [20]. It is worth mentioning here, that the compound was earlier reported to show polymorphism with different crystal structures, viz., cubic (space group $F\bar{4}3m$) [21,22], trigonal (space group $P3m1$) [23] and hexagonal (space group $P6_3/mmc$) [19,20]. Among these, the noncentrosymmetric trigonal structure hosts a stable Néel-type skyrmion over a wide temperature range [23]. Studies on the hexagonal polymorphs at low temperatures uncover the realization of the long-range magnetic order which can lead to less symmetric structure, like $Amm2$ or $C2/m$ [20]. In the present study, we revisited the AHE on a high-quality single crystal of MnPtGa that crystallized in the hexagonal structure. We have used the *ab initio* calculations to correlate the sign reversal of the AHC with the electronic band structure modification due to the temperature dependence of the magnetic order.

II. METHODS

A. Experimental details

MnPtGa single crystals were grown by the modified Bridgman method. High purity Mn, Pt, and Ga were taken in the stoichiometric ratio and placed in a point-bottom alumina crucible that was baked overnight under vacuum at 1200 °C. The crucible was then sealed under a vacuum of ($\approx 10^{-5}$ mBar) inside a quartz ampoule. The sealed ampoule was placed in a box type resistive heating furnace and heated to 1100 °C and held at this temperature for 24 h to achieve proper homogenization. Then the furnace was slowly cooled down to 800 °C over a period of about two weeks. After cooling down to room temperature, the crystals were extracted by breaking the sealed quartz ampoule. Powder x-ray diffraction (XRD) measurement has been performed using the PANalytical x-ray diffractometer, equipped with a monochromatic Cu-K_α ($\lambda = 1.5406$ Å) x-ray source at room temperature. Single crystal x-ray diffraction (SXRD) data were collected using a four-circle Bruker diffractometer employing Mo-K_α radiation at around 300 K. Diffracted x rays were detected by a Bruker CCD detector where the crystal-to-detector distance was 50 mm resulting in a resolution of the SXRD data of approximately $(\sin\theta/\lambda)_{\max} = 0.802$ Å^{-1}. The diffracted intensity was collected on the detector during rotation of the crystal by 0.5°. Obtained cell parameters are $a = b = 4.334(8)$ Å and $c = 5.583(9)$ Å. The crystals were oriented, along the principal crystallographic directions, using the Laue diffraction technique and cut using a spark erosion electric discharge machine (EDM). Magnetic measurements were performed in a SQUID-VSM magnetometer (Quantum Design, USA) and electrical measurements were done in physical property measurement system (PPMS, Quantum Design).

B. SXRD analysis

To establish the correct structural model, single-crystal x-ray diffraction (SXRD) has been performed at room temperature, where we have three refinements categorized into three models corresponding to centrosymmetric and acentric space groups. In the Model A, the structure was refined employing the centrosymmetric space group $P6_3/mmc$ and in the Models B and C, the acentric space groups $P6_3mc$ and $P3m1$ were used as shown in Tables ST1 and ST2 in the Supplemental Material (SM) [24]. One can see that upon choosing the acentric space groups $P6_3mc$ and $P3m1$ (Models B and C), we have more degrees of freedom for the refinement, thereby increasing the number of parameters. However, even with the extra parameters the fit did not improve making it hard to justify the model with the acentric hexagonal or trigonal space groups as opposed to the centrosymmetric hexagonal space group $P6_3/mmc$. Moreover, for Models B and C with the acentric space groups, the z coordinate (see tables in the SM [24]) is no longer constrained by symmetry as it was in the centrosymmetric hexagonal setting. Upon refining z, the standard uncertainty was quite large, thereby making it unreliable. Hence, Model A has been identified as the best to describe the structure in the present case.

C. Computational details

The first-principles density functional theory (DFT) calculations were performed using the projector augmented-wave (PAW) potentials [25] implemented in the Vienna *ab initio* simulation package (VASP) code [26–28]. For the exchange-correlation energy, the generalized gradient approximation (GGA) in the Perdew, Burke, and Ernzerhof (PBE) parametrization was used [29]. The energy cutoff for the plane-wave expansion was set to 400 eV. Optimizations of the lattice constant and atom positions (in the presence of the spin-orbit coupling) were performed using $10 \times 10 \times 8$ **k**-point grid, using the Monkhorst-Pack scheme [30].

Direct DFT calculations were used in the calculation of tight binding model in the maximally localized Wannier orbitals [31–33], constructed by WANNIER90 [34] software. We also performed calculations with the fixed values and directions of Mn magnetic moment (I_CONSTRAINED tag). Similar technique was earlier used to study of the doping effect on the AHE in thin ferromagnetic film $Sr_{1-x}Ca_xRuO_3$ [15].

As a convergence condition of the optimization loop, we took the energy change below 10^{-6} and 10^{-8} eV for ionic and electronic degrees of freedom. The obtained optimized structure were examined in context of the dynamical stability, via phonon spectrum calculation (calculations include the spin-orbit coupling). We used the direct *Parlinski-Li-Kawazoe* method [35], implemented in the PHONOPY software [36,37]. The crystal symmetry was analysed using FINDSYM [38] and SPGLIB [39], while the momentum space analysis was done using SEEK-PATH tools [40].

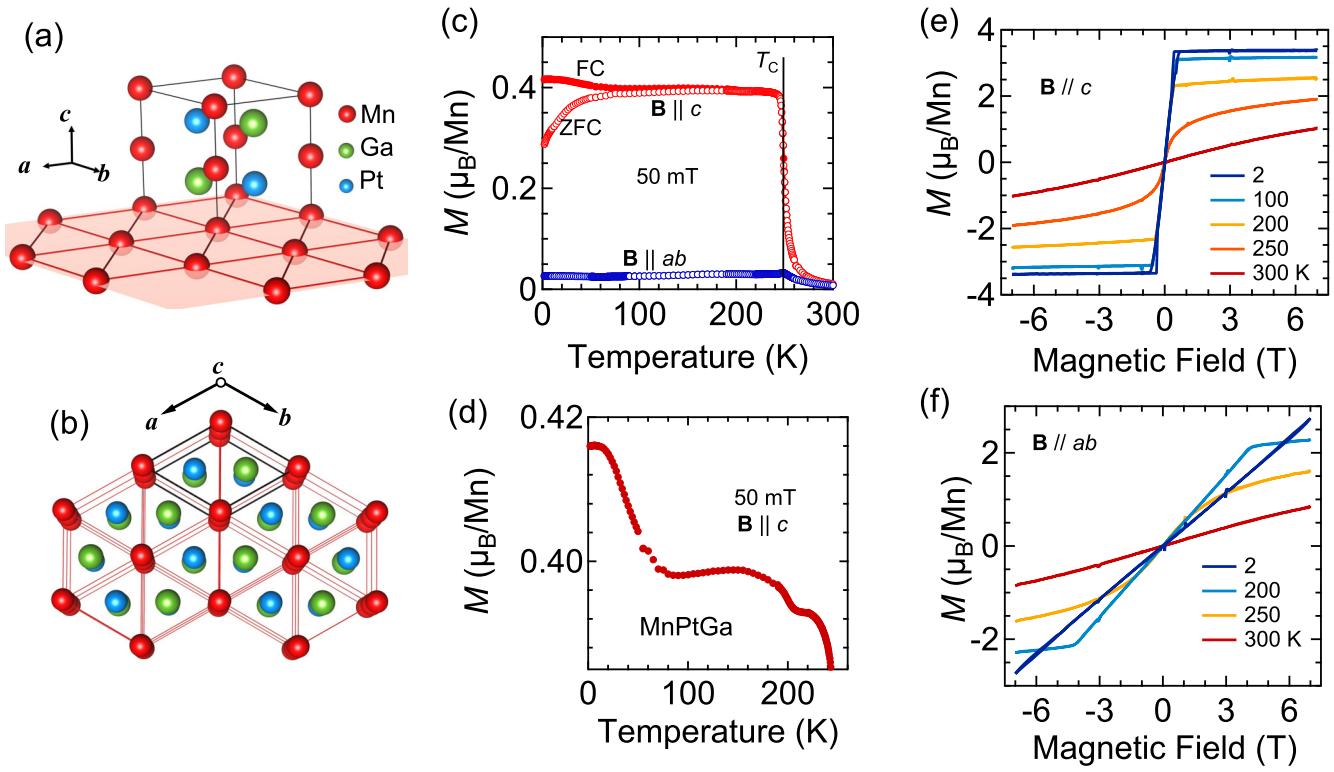

FIG. 1. Structure and magnetization of MnPtGa. [(a) and (b)] Centrosymmetric crystal structure of MnPtGa where red, green, and blue balls represent the Mn, Ga, and Pt atoms, respectively. (c) Temperature dependence of magnetization M with FC and ZFC protocols for 50 mT magnetic field applied along c direction and in ab plane. (d) Enlarged M vs T for field in c direction with FC protocol, depicting multiple magnetic transitions. Isothermal magnetization M at selected temperatures $B\|c$ and $B\|ab$ plane are depicted in (e) and (f), respectively.

III. RESULTS AND DISCUSSIONS

A. Structural analysis

As MnPtGa shows polymorphism with three different crystal structures, it is crucial to determine that in which polymorphic form our Bridgman-grown MnPtGa has crystallized into [19–23]. We have used powder x-ray diffraction and the Laue technique (see Figs. SF1(a) and SF1(b) in the SM [24]) as a preliminary tool of identification that clearly rules out the cubic structure. It is to be noted that polycrystalline material synthesized by arc melting is reported to adopt the Ni_2In structure type described by the space group $P6_3/mmc$ as shown in Figs. 1(a) and 1(b), where its characteristic feature is a honeycomb lattice involving a stacking of Mn with Pt-Ga atoms along the c direction (ABAB fashion) [20]. However, in one of the recent reports, the single crystals grown by Bridgman method was reported to crystallize in $P3m1$ trigonal space group breaking the sixfold symmetry [23]. This results in an acentric structure defined by the polar space group $P3m1$, which is essentially a sub-group of $P6_3/mmc$ following the Bärnighausen formalism. With the acentric structure, there are three additional atoms: Mn, Pt, and Ga split into two, where the site symmetry is also $3m$ for the new atoms (see Table ST2 in the SM [24]). However, single crystal x-ray diffraction (SXRD) analysis (see *Methods*) on our sample suggests that the center of inversion is still present in the crystal structure. This is reinforced by no improvement to the model by refinement of additional parameters for the acentric $P3m1$, where the Flack parameter was also refined by treating it as an inversion twin that resulted in an unphysical value of $-0.1(2)$, which is also similar to the Model B refinement employing $P6_3mc$. Moreover, absence of the $l = 2n + 1$ reflections in the reciprocal layers of h0l and hhl unequivocally shows that the crystal structure is centrosymmetric $P6_3/mmc$ (see Tables ST1 and ST2 in the SM [24] for details).

B. Magnetic properties

Measurement of magnetization as a function of temperature $[M(T)]$ in 0.05 T magnetic field [Fig. 1(c)] applied both in-plane and out-of-plane directions, demonstrates that MnPtGa undergoes a ferromagnetic transition at $T_C = 250$ K. However, when the temperature is further lowered MnPtGa enters into a spin-canted state at around $\approx$165 K (T_0) indicated by the broad hump for field along both the principal crystallographic directions (see Figs. 1(d) and SF3(d) in the SM [24]). From powder neutron diffraction experiments, the spin-canted state can be understood as the resultant of two components: a ferromagnetic component along the c direction together with an antiferromagnetic moment pointed in the a direction [20]. Additional kinks in $M(T)$ when lowering the temperature suggest a rich magnetic structure that evolves with temperature. Moreover, magnetostriction studies [20] have shown that these transitions are coupled with the lattice and lead to negative volume magnetostriction in MnPtGa. Our field-dependent magnetization $[M(B)]$ measurements suggest

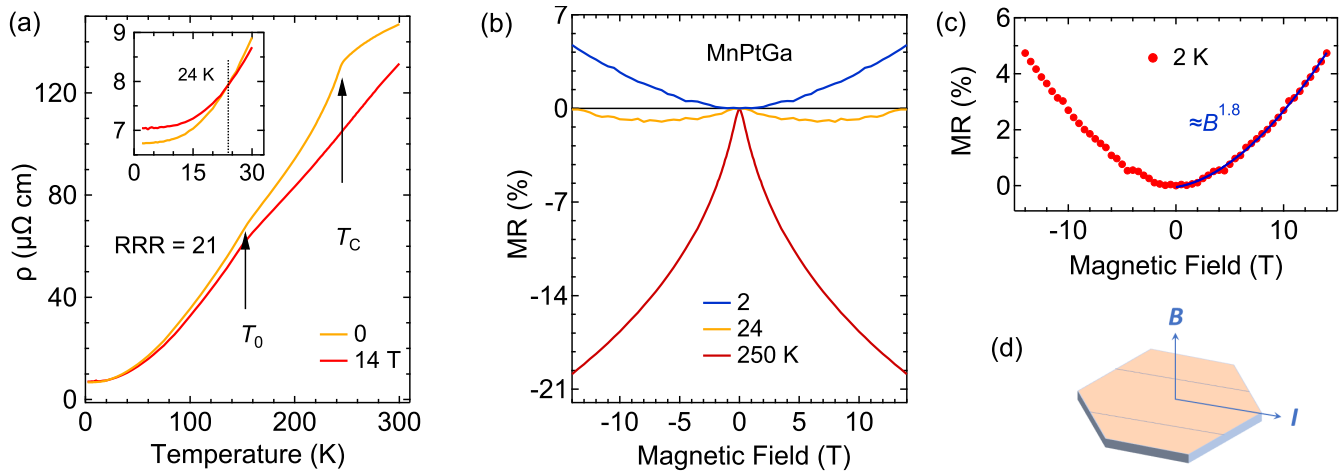

FIG. 2. Linear resistivity and magnetoresistance of MnPtGa. (a) ρ vs temperature at 0 and 14 T magnetic field applied along c axis (left axis) and temperature derivative of ρ at 0 T (right axis) indicating the ferromagnetic Curie temperature T_C and T_0 at which the canting of the spins occur. Inset shows a crossover point around 24 K below which the magnetoresistance becomes negative to positive at 14 T. (b) Magnetic field dependence of magnetoresistance, MR, at three selected temperatures of 2, 24, and 250 K. (c) Positive MR of MnPtGa at 2 K fitted with a power law with exponent 1.8. (d) Schematic of the current and applied magnetic field used to measure linear resistivity.

that MnPtGa is a soft ferromagnet with strong magnetocrystalline anisotropy. The saturation field (≈0.5 T) is fairly low along the c axis [Fig. 1(e)] and extremely large (≈8.5 T) in the ab plane [Fig. 1(f)], at 2 K, confirming dominant out-of-plane magnetization. However, unlike the thin film and polycrystalline MnPtGa [18,20], we found negligible coercivity in the single crystalline form indicating a rather soft ferromagnetic nature. Experimentally observed saturation magnetization is almost constant in a wide temperature range (≈2–50 K) with a value of 3.3 μ_B/Mn which is very close to the theoretical moment of 3.6 μ_B/Mn, implying a complete field polarized state is achieved by applying ≈0.5 T magnetic field in the out-of-plane direction.

Additionally, we performed the theoretical calculations for different Mn-magnetic moment orientations (i.e. magnetic moments along c, and tilted from c axis) [18,19]. These findings support previous studies of the magnetic order in MnPtGa [18,19]. The calculated magnetic anisotropy energy (MAE) is around 0.9 meV/f.u., while the estimated magnetic moment amounts to 3.6 μ_B. A similar value of the magnetic moment was observed in a previous theoretical investigation by Cooley *et al.,* [20]. However, this theoretically estimated value of the ordered moment is slightly higher than the experimentally observed one. This difference can be related to realization long-range magnetic order at low temperatures, due to the combination of canted-spin order and spin density wave [20]. Moreover, from optimization of the crystal structure with different magnetic moment, we found that the emergence of noncollinear magnetic order (with tilted magnetic state) can lead to the local symmetry breaking, and lowering of the crystal structure. Nevertheless, such "local" symmetry breaking does not affect the system stability (see Sec. SS3 in the SM [24]), while it can affect the global electronic properties of the system with long-range magnetic order [20].

C. Linear and Hall resistivity

As evident from the longitudinal electrical resistivity (ρ_{xx}) of MnPtGa, shown in Fig. 2(a), we have grown a high-quality single crystal with a residual resistivity ratio (RRR) of ≈ 22 reflecting a coherent growth and good quality of the single crystal. MnPtGa exhibits a metal-like behavior where the resistivity decreases with decreasing temperature with a sharp drop below T_C due to a reduction in the spin-disordered scattering. Additionally, a broad hump around T_0 indicates the onset of the canted magnetic state. As the field is ramped up to 14 T, a negative magnetoresistance with large value at T_C, is observed over a large temperature range that is typical for ferromagnetic metals. However, the hump around T_0 persists even at 14 T. This confirms that the transition at T_0 has structural origin as well indicated by the magnetostriction analysis in the previous study [20].

When the temperature is further lowered, the negative magnetoresistance becomes progressively smaller, and a crossover is observed where the magnetoresistance changes sign and becomes positive below 24 K, shown in the inset of Fig. 2(a). This is also evident from Fig. 2(b) where field-dependent magnetoresistance is plotted. At 24 K, the MR has distinct features: near zero field, MR decreases with increasing magnetic field but beyond 7 T, it increases boundlessly, indicating the crossover temperature is not constant but varies with the applied magnetic field. At 2 K MR is completely positive and increases without any saturation up to a magnetic field of 14 T. An attempt to fit the MR data at 2 K with $MR \sim B^n$ yielded an exponent value of 1.8. To further investigate this behavior, we have used the semiclassical two-band model to fit $\rho_{xx}(B)$ and $\rho_{xy}(B)$ simultaneously for fields above 3 T where the anomalous term (c) in $\rho_{xy}(B)$ can be considered as constant:

$$\rho_{xy} = c + \frac{1}{e}\left[\frac{(n_h\mu_h^2 - n_e\mu_e^2)B + (n_h - n_e)\mu_h^2\mu_e^2B^3}{(n_h\mu_h + n_e\mu_e)^2 + (n_h - n_e)^2\mu_h^2\mu_e^2B^2}\right], \quad (1)$$

Extracted mobilities are $\mu_e = 1.61(8) \times 10^2$ cm^2 V^{-1} s^{-1} and $\mu_h = 1.48(7) \times 10^2$ cm^2 V^{-1} s^{-1} for electrons and holes, with carrier densities $n_e = 2.61(9) \times 10^{21}$ cm^{-3} and $n_e = 3.40(6) \times 10^{21}$ cm^{-3}, respectively, which is one order of magnitude smaller than the reported carrier density in MnPtGa

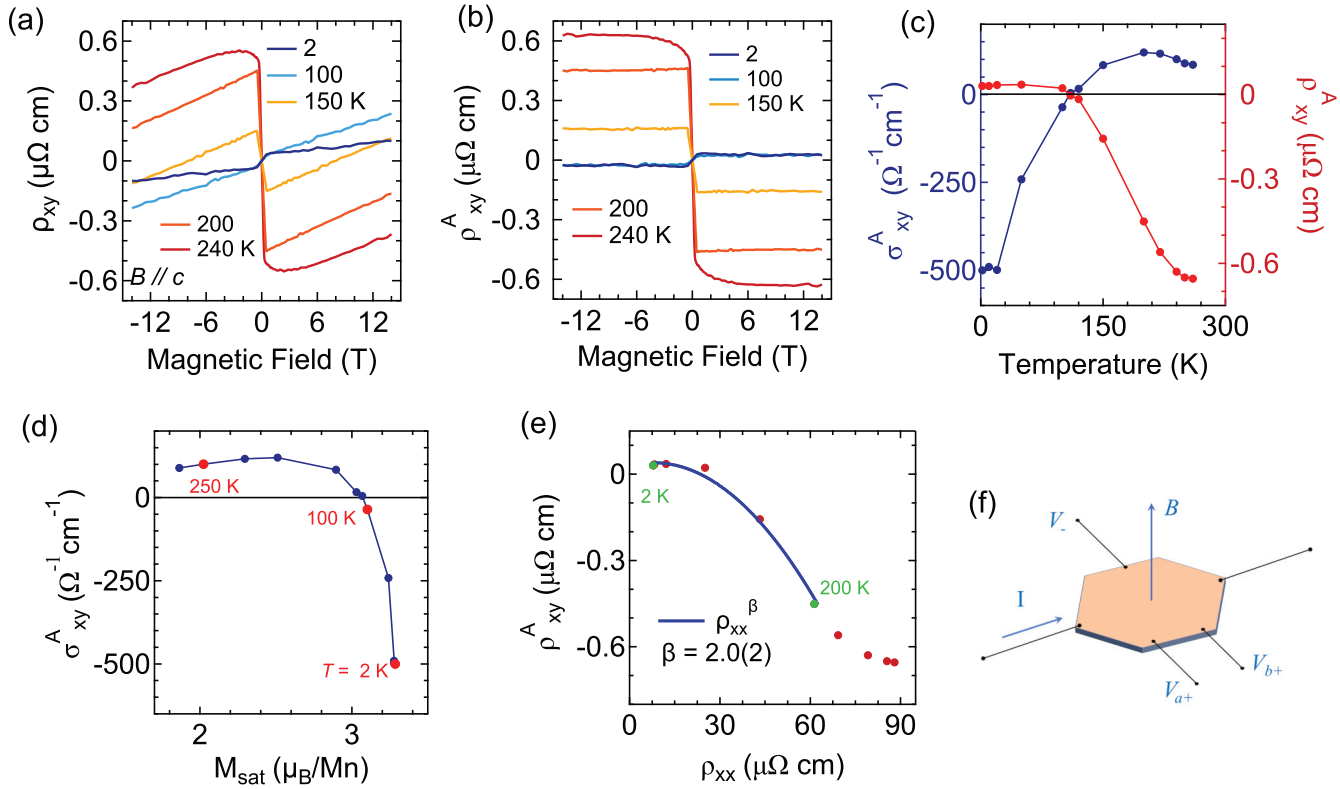

FIG. 3. Hall effect in MnPtGa. (a) Antisymmetrized ρ_{xy} vs B and (b) ρ^A_{xy} vs B at different temperatures. (c) T dependence of σ^A_{xy} (left axis) and ρ^A_{xy} (right axis) at zero magnetic fields, depicting the sign reversal of AHE. (d) Plot of σ^A_{xy} vs saturated magnetization $M_{\rm sat}$. (e) Plot of ρ^A_{xy} vs ρ_{xx} with temperature as a parameter. The solid line represents the fitting with $\rho^A_{xy} \propto (\rho_{xx})^\beta$ relation. (f) Schematic diagram of sample geometry along with current and applied magnetic field directions.

thin film. Small values of mobilities also justify the negligible magnetoresistance at 2 K.

Our transport measurements reveal a robust signature of the anomalous Hall effect for out-of-plane configuration of $I \| [1\bar{2}10]$ and $B \| [0001]$ but vanish for in-plane field directions. Total Hall resistivity (ρ_{xy}) of MnPtGa can be decomposed into two parts:

$$\rho_{xy} = R_0 B + \rho^A_{xy} \tag{2}$$

where the first term denotes the ordinary Hall contribution (ρ^O_{xy}) due to Lorentz force and ρ^A_{xy} is the anomalous Hall resistivity. As anomalous Hall resistivity is proportional to the magnetization M of the sample, ρ^A_{xy} becomes also constant beyond the saturation of M, thus a linear fitting will produce the intercept as anomalous Hall term with the slope as R_0. The linear behavior of normal Hall can be justified from Eq. (1), where for $n_e \cong n_h$, the B^3 and B^2 terms from numerator and denominator become negligible and ρ_{xy} reduces to linear in B, that is observed in MnPtGa above the field where M is saturated. From the plot of the magnetic field variation of ρ^A_{xy}, in Fig. 3(b), we observe that ρ^A_{xy} is negative around T_C but becomes positive when lowering the temperature. We have also estimated temperature dependence of σ^A_{xy} at zero field from the ρ^A_{xy} and ρ_{xx} data ($\sigma^A_{xy} = -\rho^A_{xy}/(\rho^2_{xx} + \rho^{A\,2}_{xy})$) which depicts a sign change at around 109 K (T^*). A similar behavior has also been observed in the thin film of MnPtGa [18].

The observed anomalous Hall effect can be dominated either by extrinsic impurity scattering or by intrinsic mechanisms. To investigate the underlying mechanism, we have plotted ρ^A_{xy} versus ρ_{xx} and fitted the data to a power law behavior as shown in Fig. 3(e) which yields the exponent $\beta = 2.0$. This rules out the presence of the skew-scattering mechanism, which is well known to vary linearly with ρ_{xx}. The observed quadratic behavior suggest that the extrinsic side-jump or intrinsic Berry curvature mechanism may be responsible for the observed AHE in MnPtGa [19].

AHC for the side-jump contribution in multiband ferromagnets with dilute impurity can be estimated from the expression, $(e^2/(ha)) \cdot (\epsilon_{SO}/E_{\rm F})$, where ϵ_{SO} is the spin-orbit interaction energy, and a is the lattice constant [41]. Using the lattice constant, $a \sim V^{1/3} = 4.495$ Å and estimated $\epsilon_{SO}/E_{\rm F} \sim 0.01$, the derived side-jump contribution is 8.6 Ω^{-1} cm^{-1}, which is very small compared to the observed AHC. A similar value has been obtained in ferromagnetic half metal $Co_3Sn_2S_2$ for side-jump contribution [9]. Moreover, the longitudinal conductivity (σ_{xx}) of MnPtGa lies in the intermediate regime ($2 \times 10^3 < \sigma_{xx} < 6 \times 10^5$ Ω^{-1} cm^{-1}) which indicates AHC of MnPtGa is neither dominated by skew scattering (high conductivity regime, $\sigma_{xx} > 6 \times 10^5$ Ω^{-1} cm^{-1}) nor by impurity scattering (bad metal hopping region, $\sigma_{xx} < 2 \times 10^3$ Ω^{-1} cm^{-1}). However, our observation from the temperature dependence of the σ^A_{xy} plot suggests that below 20 K (below the crossover temperature), σ^A_{xy} becomes nearly

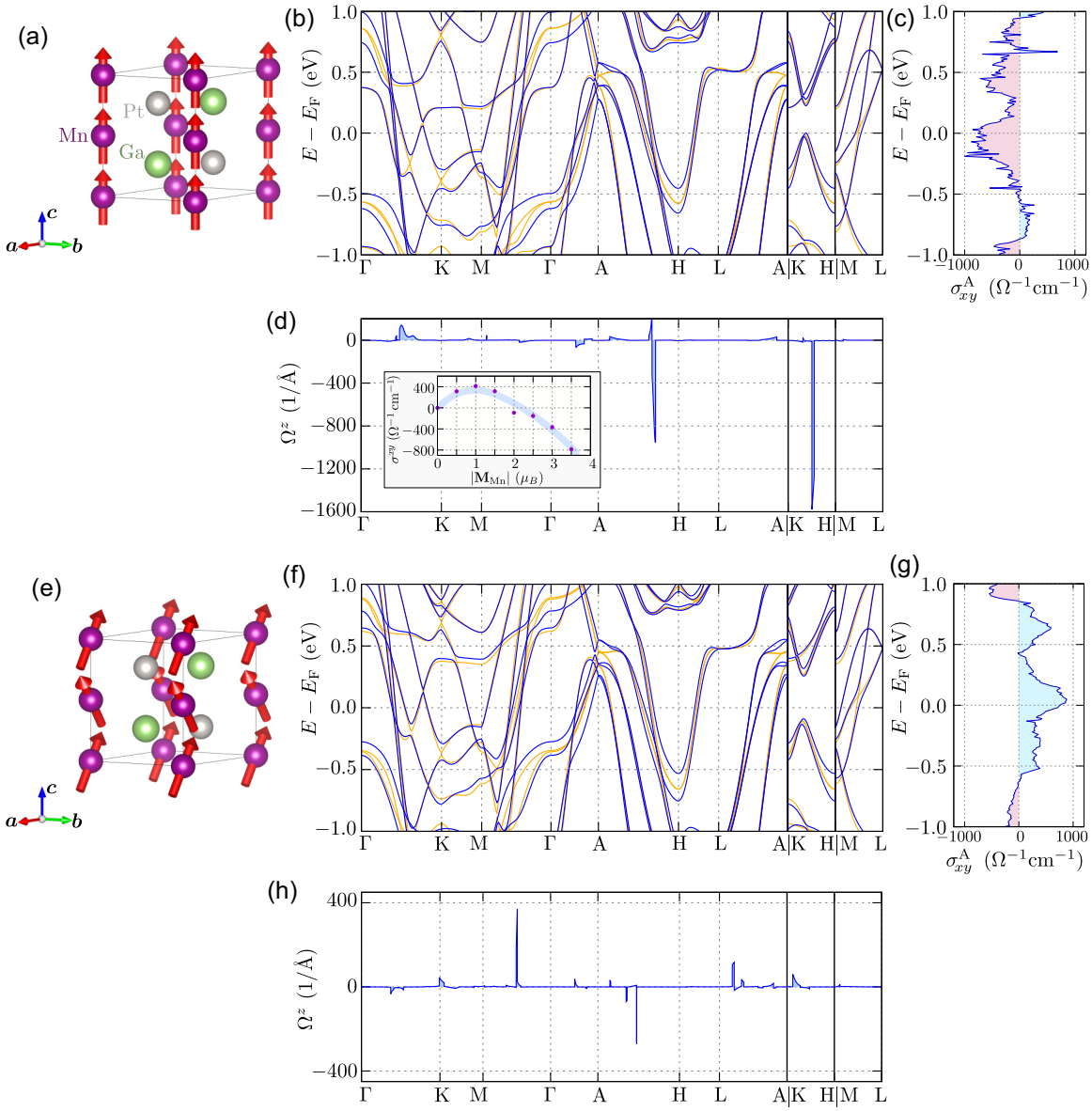

FIG. 4. The influence of the magnetic order on the electronic transport properties of MnPtGa. Top panels (a)–(d) and bottom panels (f)–(h) present results for the Mn magnetic moment along c direction (a) and tilted from c direction (e), respectively. The electronic band structure [(b) and (f)], the Berry curvature $\Omega_z(k)$ on the Fermi level along high symmetry directions [(c) and (g)] and the Fermi level dependence of AHE σ^A_{xy} [(d) and (h)]. Inset on (d), present magnetic moment dependence of AHE σ^A_{xy}.

constant. This behavior of σ^A_{xy} is also observed in the anomalous Hall compound $Co_3Sn_2S_2$ (for example) in a wider range of temperature below 100 K which agrees with the prediction of the unified model for AHE physics for the intrinsic anomalous Hall effect [10]. Collectively, these indicate that the observed anomalous Hall effect in MnPtGa is originating from the intrinsic mechanism dominated by the Berry curvature.

D. Electronic band structure

We have performed a detailed electronic structure study to investigate the proposed mechanism of AHE based on experimental results. Theoretical calculations, assuming full optimization of the system, uncover the ground state with the magnetic moment tilted from the c-direction. However, tilting of the magnetic moment leads to the breaking of the symmetry resulting in a lower symmetry $P2_1/m$ (see Sec. SS3 in the SM [24]). Contrary to this, the Mn magnetic moments along c direction preserved the $P6_3/mmc$ symmetry. Both structures are stable in a dynamic sense and can be used to mimic "true" structures at different temperatures. As mentioned earlier, the experimental investigation related to the low-temperature long-range magnetic order [20], suggests the realization of a magnetic unit cell with symmetry $C2/m$ (around 10 K) or $Amm2$ (around 50 K). Indeed, the low-temperature magnetic unit cell can be understood as a combination of both magnetic orders (with magnetic moment along c-direction and tilted from c direction). Accordingly, results for systems with Mn magnetic moments along the c direction and tilted from the c direction can be used to explain the reported results (Fig. 4).

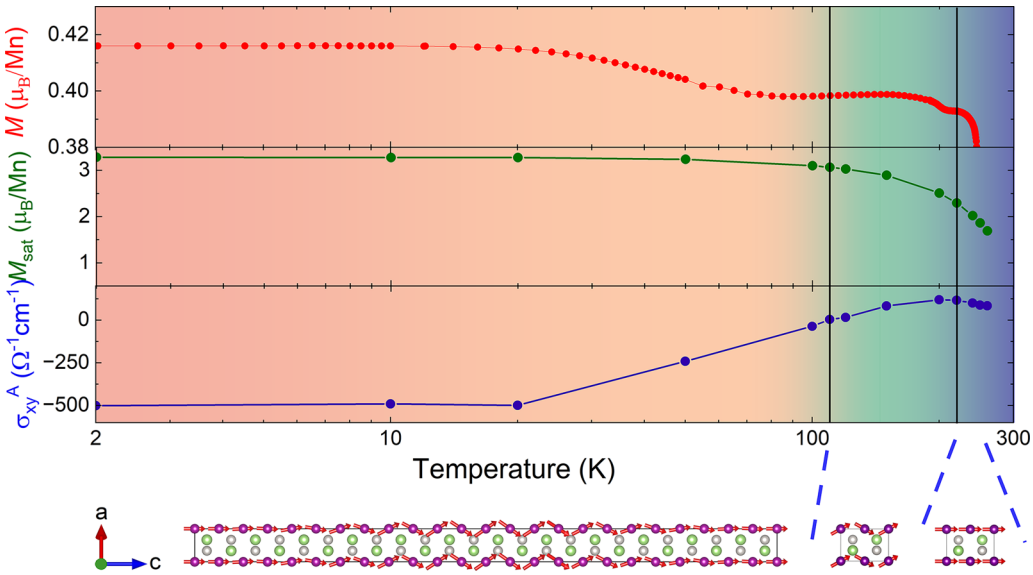

FIG. 5. The evolution of magnetization (measured in a field 50 mT), saturation magnetization, and anomalous Hall conductivity of MnPtGa with temperature, for $B \parallel c$. Cartoons of different magnetic structures at corresponding temperature ranges are also shown at the bottom panel.

The electronic band structure in the absence and presence of the spin-orbit coupling for the magnetic moments along c direction and tilted from c direction are shown in Figs. 4(a) and 4(d), respectively. In the absence of spin-orbit coupling, several band crossings can be found in the vicinity of the Fermi level for both magnetic orders. Introducing this spin-orbit coupling leads to the opening of well-visible band gaps in the electronic band structure (cf. orange and blue lines on Figs. 4(d) and 4(h), see also Fig. SF5 in the SM [24]). Arising spin-mixing states around this gap contribute to the large Berry curvature [4,42]:

$$\Omega_n^z(\boldsymbol{k}) = -2\hbar^2 \mathrm{Im} \sum_{m \neq n} \frac{\langle \Psi_{n\boldsymbol{k}} | v_x | \Psi_{m\boldsymbol{k}} \rangle \langle \Psi_{m\boldsymbol{k}} | v_y | \Psi_{n\boldsymbol{k}} \rangle}{(E_{m\boldsymbol{k}} - E_{n\boldsymbol{k}})^2}, \quad (3)$$

where $v_{x(y)}$ is the velocity operator, while $E_{n\boldsymbol{k}}$ and $\langle \Psi_{n\boldsymbol{k}}$ eigenpair of nth band at momentum $\boldsymbol{k}$. When $E_{m\boldsymbol{k}}$ is close to $E_{n\boldsymbol{k}}$, then large Berry curvature emerge. Indeed, this is clear in Figs. 4(b) and 4(e), where the z component of the Berry curvature Ω^z at the Fermi level is presented. It is important to highlight that the alteration of the magnetic order, achieved by tilting the Mn magnetic moments away from the c direction, resulted in a substantial modification of the obtained results, as illustrated in Figs. 4(f)–4(h).

The nonvanishing total Berry curvature over the Brillouin zone gives rise to the AHE with $\sigma_{xy}^A \sim \int_{\mathrm{BZ}} d^3\boldsymbol{k} \sum_n f_n(E_{n\boldsymbol{k}}) \Omega_z^n(\boldsymbol{k})$, where $f_n(E)$ is the Fermi-Dirac distribution, and n is the index of the occupied bands [see Figs. 4(c) and 4(g)]. Here we would like to mention, that the electronic properties strongly depend on the Mn magnetic moment direction. In particular, tilting of the Mn magnetic moment from the c-direction leads to the change of the AHE sign, [cf. Figs. 4(c) and 4(g)]. The link between theoretically obtained structures and experimentally observed magnetic order uncovers a mechanism leading to the change of sign in MnPtGa with temperature [presented in Fig. 3(c)]. For example, at the high-temperature phase, when the magnetic moment is titled from the c direction [20], the AHC is positive. Conversely, decreasing the temperature results in the stabilization of long-range magnetic order, particularly affecting the phase with magnetic order along the c-direction [illustrated by negative AHE in Fig. 3(c)]. From this, decreasing temperature leads to the change in AHE sign to negative (Fig. 5). A similar effect was reported in $Sr_{1-x}Ca_xRuO_3$ series ($0 \leqslant x \leqslant 0.4$) [15], where the AHE changed sign with temperature during the modification of magnetic moment. In this context, the present situation becomes more intricate as lowering the temperature results in both modifications to the magnetic order and a change in the sign of AHE. Indeed, the AHE sign change is observed around the temperature, where low-temperature long-range magnetic order emerges.

IV. SUMMARY AND CONCLUSIONS

One of the less explored and most exciting phenomena in the field of AHE is probably the sign reversal of AHC, which we have studied in this article in the spin-canted magnet MnPtGa using magneto-transport measurements and theoretical investigations. The scaling behavior of ρ_{xy}^A with ρ_{xx} together with the unified model of AHE, we conclude that the observed AHE in MnPtGa originates from the momentum space Berry curvature. A complex magnetic structure has been substantiated by our magnetization measurements. We have estimated the temperature dependence of σ_{xy}^A from the first principle calculation by considering the temperature dependence of the Bloch state exchange splitting which is proportional to the temperature evolution of magnetization. To voice our experimentally observed sign reversal of σ_{xy}^A, we have used *ab initio* calculations, $M(T)$ data, and magnetic structures determined from neutron diffraction (from Refs. [19,20]). For easy understanding, we have split the complete temperature range into three slices (Fig. 5): (i) for $T > 220$ K, the system is in the ferromagnetic state with

relatively low magnitude of magnetic moments, aligned along c axis. In this temperature range, experimental σ_{xy}^{A} is positive. Our calculated σ_{xy}^{A} [see inset of Fig. 4(d)] also depicts a positive value when magnetization goes below $\approx 2\ \mu_B$ which corresponds to near T_C. (ii) In 110 K $< T <$ 220 K range, the canted magnetic state becomes more stable, which is evident from neutron diffraction and the downturn of $M(T)$ data as the temperature is lowered. The calculated AHC also exhibits a positive value in the canted magnetic state, which follows our experimental results. (iii) As the temperature is further lowered, there is competition between ferromagnetic and canted magnetic interactions. However, our $M(T)$ data exhibit a ferromagnetic type upturn indicating a dominant ferromagnetic interaction, which leads to a negative sign of σ_{xy}^{A}. In Refs. [19,20], it was established from the ND study, that the magnetic ground state at low temperatures is stabilized with a combined canted AFM and spin density wave structure, with a large magnitude of the magnetic moment among crystallographic $c-$direction. In the present study, we calculated the AHE considering the FM state (i.e., with a large magnitude of the magnetic moment along c direction) and obtained a negative value of σ_{xy}^{A}, which justifies our results. Thus, according to our proposed model, the anomalous sign reversal of the anomalous Hall conductivity (AHC) in this compound is governed by both the magnitude of the magnetic moment and the underlying magnetic interaction.

ACKNOWLEDGMENTS

The crystal structures in Figs. 1, 4, and 5 were rendered using VESTA software [43]. We kindly acknowledge support from the National Science Centre (NCN, Poland) under Project No. 2021/43/B/ST3/02166. A.P. is grateful to Laboratoire de Physique des Solides in Orsay (CNRS, University Paris Saclay) for hospitality during a part of the work. P.P.J. would like to thank the Science & Engineering Research Board (SERB), India, for Core Research Grant CRG/2020/004115.

[1] N. Nagaosa, J. Sinova, S. Onoda, A. H. MacDonald, and N. P. Ong, Anomalous Hall effect, Rev. Mod. Phys. **82**, 1539 (2010).
[2] T. Jungwirth, Q. Niu, and A. H. MacDonald, Anomalous Hall effect in ferromagnetic semiconductors, Phys. Rev. Lett. **88**, 207208 (2002).
[3] M. Onoda and N. Nagaosa, Quantized anomalous Hall effect in two-dimensional ferromagnets: Quantum Hall effect in metals, Phys. Rev. Lett. **90**, 206601 (2003).
[4] Y. Yao, L. Kleinman, A. H. MacDonald, J. Sinova, T. Jungwirth, D.-S. Wang, E. Wang, and Q. Niu, First principles calculation of anomalous Hall conductivity in ferromagnetic bcc Fe, Phys. Rev. Lett. **92**, 037204 (2004).
[5] J. Smit, The spontaneous Hall effect in ferromagnetics I, Physica **21**, 877 (1955).
[6] J. Smit, The spontaneous Hall effect in ferromagnetics II, Physica **24**, 39 (1958).
[7] L. Berger, Side-jump mechanism for the Hall effect of ferromagnets, Phys. Rev. B **2**, 4559 (1970).
[8] R. Karplus and J. M. Luttinger, Hall effect in ferromagnetics, Phys. Rev. **95**, 1154 (1954).
[9] Q. Wang, Y. Xu, R. Lou, Z. Liu, M. Li, Y. Huang, D. Shen, H. Weng, S. Wang, and H. Lei, Large intrinsic anomalous Hall effect in half-metallic ferromagnet $Co_3Sn_2S_2$ with magnetic Weyl fermions, Nat. Commun. **9**, 3681 (2018).
[10] E. Liu, Y. Sun, N. Kumar, L. Muechler, A. Sun, L. Jiao, S.-Y. Yang, D. Liu, A. Liang, Q. Xu, J. Kroder, V. Süß, H. Borrmann, C. Shekhar, Z. Wang, C. Xi, W. Wang, W. Schnelle, S. Wirth, Y. Chen *et al.*, Giant anomalous Hall effect in a ferromagnetic kagome-lattice semimetal, Nat. Phys. **14**, 1125 (2018).
[11] Y. Zhang, Y. Yin, G. Dubuis, T. Butler, N. V. Medhekar, and S. Granville, Berry curvature origin of the thickness-dependent anomalous Hall effect in a ferromagnetic Weyl semimetal, npj Quantum Mater. **6**, 17 (2021).
[12] K. Kim, J. Seo, E. Lee, K.-T. Ko, B. Kim, B. G. Jang, J. M. Ok, J. Lee, Y. J. Jo, W. Kang *et al.*, Large anomalous Hall current induced by topological nodal lines in a ferromagnetic van der Waals semimetal, Nat. Mater. **17**, 794 (2018).
[13] J. Chen, X. Xu, H. Li, T. Guo, B. Ding, P. Chen, H. Zhang, X. Xi, and W. Wang, Large anomalous Hall angle accompanying the sign change of anomalous Hall conductance in the topological half-Heusler compound HoPtBi, Phys. Rev. B **103**, 144425 (2021).
[14] K. S. Takahashi, H. Ishizuka, T. Murata, Q. Y. Wang, Y. Tokura, N. Nagaosa, and M. Kawasaki, Anomalous Hall effect derived from multiple Weyl nodes in high-mobility $EuTiO_3$ films, Sci. Adv. **4**, eaar7880 (2018).
[15] R. Mathieu, A. Asamitsu, H. Yamada, K. S. Takahashi, M. Kawasaki, Z. Fang, N. Nagaosa, and Y. Tokura, Scaling of the anomalous Hall effect in $Sr_{1-x}Ca_xRuO_3$, Phys. Rev. Lett. **93**, 016602 (2004).
[16] L. Shlyk, R. Niewa, and L. E. De Long, Anomalous Hall effect in the high-temperature ferrimagnetic semiconductors $BaFe_{2\pm x}Ru_{4\mp x}O_{11}$, Phys. Rev. B **82**, 134432 (2010).
[17] W.-L. Lee, S. Watauchi, V. L. Miller, R. J. Cava, and N. P. Ong, Dissipationless anomalous Hall current in the ferromagnetic spinel $CuCr_2Se_{4-x}Br_x$, Science **303**, 1647 (2004).
[18] R. Ibarra, E. Lesne, B. Sabir, J. Gayles, C. Felser, and A. Markou, Anomalous Hall effect in epitaxial thin films of the hexagonal Heusler MnPtGa noncollinear hard magnet, Adv. Mater. Interfaces **9**, 2201562 (2022).
[19] R. Ibarra, E. Lesne, B. Ouladdiaf, K. Beauvois, A. S. Sukhanov, R. Wawrzyczak, W. Schnelle, A. Devishvili, D. S. Inosov, C. Felser, and A. Markou, Noncollinear magnetic order in epitaxial thin films of the centrosymmetric MnPtGa hard magnet, Appl. Phys. Lett. **120**, 172403 (2022).
[20] J. A. Cooley, J. D. Bocarsly, E. C. Schueller, E. E. Levin, E. E. Rodriguez, A. Huq, S. H. Lapidus, S. D. Wilson, and R. Seshadri, Evolution of noncollinear magnetism in magnetocaloric MnPtGa, Phys. Rev. Mater. **4**, 044405 (2020).
[21] F. A. Hames and J. Crangle, Ferromagnetism in Heusler type alloys based on platinum group or palladium group metals, J. Appl. Phys. **42**, 1336 (1971).

[22] R. A. Dunlap, S. Jha, H. H. Seyoum, G. M. Julian, R. A. Pappas, and J. W. Blue, Hyperfine fields at sp sites in Clb Heusler alloys, Hyperfine Interact. **16**, 689 (1983).

[23] A. K. Srivastava, P. Devi, A. K. Sharma, T. Ma, H. Deniz, H. L. Meyerheim, C. Felser, and S. S. P. Parkin, Observation of robust Néel skyrmions in metallic PtMnGa, Adv. Mater. **32**, 1904327 (2020).

[24] See Supplemental Material at http://link.aps.org/supplemental/10.1103/PhysRevB.110.045111 for structural refinements using single crystal XRD, powder XRD, Laue diffraction patterns, Hall resistivity, temperature dependence of magnetization and electronic structure.

[25] P. E. Blöchl, Projector augmented-wave method, Phys. Rev. B **50**, 17953 (1994).

[26] G. Kresse and J. Hafner, *Ab initio* molecular-dynamics simulation of the liquid-metal–amorphous-semiconductor transition in germanium, Phys. Rev. B **49**, 14251 (1994).

[27] G. Kresse and J. Furthmüller, Efficient iterative schemes for *ab initio* total-energy calculations using a plane-wave basis set, Phys. Rev. B **54**, 11169 (1996).

[28] G. Kresse and D. Joubert, From ultrasoft pseudopotentials to the projector augmented-wave method, Phys. Rev. B **59**, 1758 (1999).

[29] J. P. Perdew, K. Burke, and M. Ernzerhof, Generalized gradient approximation made simple, Phys. Rev. Lett. **77**, 3865 (1996).

[30] H. J. Monkhorst and J. D. Pack, Special points for Brillouin-zone integrations, Phys. Rev. B **13**, 5188 (1976).

[31] N. Marzari and D. Vanderbilt, Maximally localized generalized Wannier functions for composite energy bands, Phys. Rev. B **56**, 12847 (1997).

[32] I. Souza, N. Marzari, and D. Vanderbilt, Maximally localized Wannier functions for entangled energy bands, Phys. Rev. B **65**, 035109 (2001).

[33] N. Marzari, A. A. Mostofi, J. R. Yates, I. Souza, and D. Vanderbilt, Maximally localized Wannier functions: Theory and applications, Rev. Mod. Phys. **84**, 1419 (2012).

[34] G. Pizzi, V. Vitale, R. Arita, S. Blügel, F. Freimuth, G. Géranton, M. Gibertini, D. Gresch, C. Johnson, T. Koretsune, J. Ibañez-Azpiroz, H. Lee, J.-M. Lihm, D. Marchand, A. Marrazzo, Y. Mokrousov, J. I. Mustafa, Y. Nohara, Y. Nomura, L. Paulatto *et al.*, WANNIER90 as a community code: new features and applications, J. Phys.: Condens. Matter **32**, 165902 (2020).

[35] K. Parlinski, Z. Q. Li, and Y. Kawazoe, First-principles determination of the soft mode in cubic ZrO_2, Phys. Rev. Lett. **78**, 4063 (1997).

[36] A. Togo, L. Chaput, T. Tadano, and I. Tanaka, Implementation strategies in phonopy and phono3py, J. Phys.: Condens. Matter **35**, 353001 (2023).

[37] A. Togo, First-principles phonon calculations with phonopy and phono3py, J. Phys. Soc. Jpn. **92**, 012001 (2023).

[38] H. T. Stokes and D. M. Hatch, FINDSYM: program for identifying the space-group symmetry of a crystal, J. Appl. Crystallogr. **38**, 237 (2005).

[39] A. Togo and I. Tanaka, SPGLIB: a software library for crystal symmetry search, arXiv:1808.01590.

[40] Y. Hinuma, G. Pizzi, Y. Kumagai, F. Oba, and I. Tanaka, Band structure diagram paths based on crystallography, Comput. Mater. Sci. **128**, 140 (2017).

[41] S. Onoda, N. Sugimoto, and N. Nagaosa, Intrinsic versus extrinsic anomalous Hall effect in ferromagnets, Phys. Rev. Lett. **97**, 126602 (2006).

[42] X. Wang, J. R. Yates, I. Souza, and D. Vanderbilt, *Ab initio* calculation of the anomalous Hall conductivity by Wannier interpolation, Phys. Rev. B **74**, 195118 (2006).

[43] K. Momma and F. Izumi, VESTA3 for three-dimensional visualization of crystal, volumetric and morphology data, J. Appl. Cryst. **44**, 1272 (2011).